MEASURING REGIONAL CHANGES IN THE DIASTOLIC DEFORMATION OF THE LEFT VENTRICLE OF SHR RATS USING MICROPET TECHNOLOGY AND HYPERELASTIC WARPING

AI Veress[1], JA Weiss[1], RH Huesman[2], BW Reutter[2], SE Taylor[2], A Sitek[5], B Feng[3], Y Yang[4], and GT Gullberg[2]

[1]THE UNIVERSITY OF UTAH
DEPARTMENT OF BIOENGINEERING, AND THE
SCIENTIFIC COMPUTING AND IMAGING INSTITUTE
SALT LAKE CITY, UT

[2]E. O. LAWRENCE BERKELEY NATIONAL LABORATORY,
LIFE SCIENCE DIVISION
BERKELEY, CA

[3]UNIVERSITY OF MASSACHUSETTS MEDICAL SCHOOL
DEPARTMENT OF RADIOLOGY,
WORCESTER, MA

[4]THE UNIVERSITY OF CALIFORNIA,
DEPARTMENT OF BIOMEDICAL ENGINEERING
DAVIS, CA

[5] HARVARD MEDICAL SCHOOL
DEPARTMENT OF RADIOLOGY
BRIGHAM AND WOMEN'S HOSPITAL
BOSTON, MA

Revision 2, Annals of Biomedical Engineering, March 22, 2008

Corresponding Author:
Alexander I. Veress
Box 352600
Seattle, WA 98195
averess@u.washington.edu
206 543-9038

Key Words:
hypertension, deformation, PET, metabolism, diastole

Condensed Title:
Hyperelastic warping analysis of microPET data from SHR and WKY Rats

Abstract

The objective of this research was to assess applicability of a technique known as hyperelastic warping for the measurement of local strains in the left ventricle (LV) directly from microPET image data sets. The technique uses differences in image intensities between template (reference) and target (loaded) image data sets to generate a body force that deforms a finite element (FE) representation of the template so that it registers with the target images. For validation, the template image was defined as the end-systolic microPET image data set from a Wistar Kyoto (WKY) rat. The target image was created by mapping the template image using the deformation results obtained from a FE model of diastolic filling. Regression analysis revealed highly significant correlations between the simulated forward FE solution and image derived warping predictions for fiber stretch (R^2 = 0.96), circumferential strain (R^2 = 0.96), radial strain (R^2 = 0.93), and longitudinal strain (R^2 = 0. 0.76) ($p<0.001$ for all cases). The technology was applied to microPET image data of two spontaneously hypertensive rats (SHR) and a WKY control. Regional analysis revealed that, the lateral freewall in the SHR subjects showed the greatest deformation compared with the other wall segments. This work indicates that warping can accurately predict the strain distributions during diastole from the analysis of microPET data sets.

Introduction

The ability to determine ventricular deformation directly from nuclear imaging data would provide a physician with valuable regional information on both diastolic and systolic cardiac function. The primary motivation for this study was the continued development of an image registration technology known as hyperelastic warping, which has the potential to be able to determine regional deformation directly from nuclear based imaging modalities. A critical step in the development of warping is validation based upon simulated images in which the deformation map depicted in the image data sets is known. The use of simulated image data based on a realistic finite element model[1] of the heart allows for direct comparison of the warping analysis with a true gold standard without confounding factors such as differences in image modalities and analysis techniques.

Diastolic heart failure is a common form of heart failure in which the heart muscle becomes stiff and shows reduced filling. Diastolic dysfunction has become a focus of study as it is thought to be a marker for myocardial damage [15-17] and may be an early compensatory response to pressure overload.[18] Studies of left ventricular (LV) diastolic chamber properties for hypertrophic hearts in humans and in animal models indicate that there is increased LV myocardial stiffness associated with diastolic dysfunction, which is likely due to fibrosis or events underlying the connective tissue response to increased loading.[19, 20] A systematic temporal study of the cardiac diastolic function in a hypertension model and the normotensive control using regional measures of deformation is needed to gain a better understanding of the mechanism(s) involved with hypertension induced heart failure.

The assessment of cardiac perfusion is commonly made using nuclear imaging as well as being used to evaluate cardiac function. Radionuclide ventriculography is one of the most widely

used techniques in the assessment of left ventricular ejection fraction (LVEF) in heart failure. Nuclear cardiac imaging systems have the capability to evaluate wall motion and wall thickening through software packages such as Quantitative Gated SPECT (QGS)[2], Perfusion and Functional Analysis for Gated SPECT (P-FAST)[3] and the Emory Cardiac Tool Box (ECTb)[4]. These packages are designed to process reconstructed gated short axis slices encompassing the entire left ventricle to obtain ejection fraction (EF), wall motion, and wall thickening. The quantification of local ventricular deformation (strain) would provide a direct measure of myocardial contraction and elongation, but these packages are currently unable to provide such measurements.

The most widely used technique for quantifying local myocardial strain is MR tagging.[5-8] The primary strength of tagging is that in vivo, noninvasive strain measurements are possible.[6, 9] The use of tagged analysis has been demonstrated in the mouse [10] so its use in the rat would be reasonable, however, to date there has not been a comprehensive temporal study of the changes in regional deformation due to pressure-overload over the lifespan of the animals as well as the deformation associated with heart failure.

Sinusas *et al.*[11] have developed a three dimensional shape-based approach for the determination of myocardial deformations from cine-MRI images. Local shape properties of the endo- and epicardial surfaces are used to track the 3-D trajectories of a dense field of these boundary points over the cardiac cycle. These trajectories are then used as boundary conditions for a subject-specific finite element model which has realistic fiber distributions and material property definitions which is used to estimate both cardiac and fiber strains in the LV. One drawback of this technique is that it is edge driven so that the strain distributions within the wall

are completely dependent upon the constitutive relation assumed for the LV and the specific material model parameters.

Hyperelastic warping allows the simultaneous determination of deformation directly from image data set through the incorporation of fiber structure into the finite element (FE) model used in the analysis.[12, 13] The intensity differences between template (reference) and target (deformed) image data set are used to deform a finite element representation of the left ventricle depicted in the template image into alignment with the target image. Image regions with large intensity gradients such as the epi- and endocardial walls as well as inhomogeneities within the wall substitute for fiducial points for the image registration. The first objective of this study was to determine if hyperelastic warping was suitable for the extraction of high-resolution strain maps of the left ventricle from microPET images of the rat left ventricle. The second objective was to determine the sensitivity of the technique to simulated changes in tracer uptake both globally (involving the entire left ventricle) and for a local wall segment in this case a region of the lateral freewall. The third objective was to determine if warping was sensitive to changes in material properties.

In addition to the validation work, an example of the applicability of this technology, warping was applied to a series of microPET images of a Wistar Kyoto (WKY) and two spontaneously hypertensive rats (SHR) to gain information about possible compensatory mechanisms in the left ventricle in response to pressure overload. The spontaneously hypertensive rat has been and continues to be a useful animal model in which to study the effects of hypertension on the heart. A valuable aspect of work using the SHR model is that long-term studies over the course of its two-year lifespan are feasible. While there are questions as to whether the SHR is a suitable model of human hypertension, the clinical course of the disease in

both animals and humans and the similarity in the response to treatment suggests that it is an appropriate model for hypertension related pathology [14].

Methods

Hyperelastic Warping Theory

Hyperelastic warping is a deformable image registration method in which a discretized FE representation of the reference, unloaded image (template) is deformed into alignment with the loaded (target) image. Specifically, the pointwise differences in image intensity and the intensity gradients, evaluated at material points in the template model are used to define body forces which deforms the mesh [21] into alignment with the target image data set. The warping analysis can incorporate the subject specific geometry, fiber distribution and material properties directly into the FE model.

A complete discussion of hyperelastic warping can be found in our previous publications [12, 13], and a synopsis is provided below. The spatially varying scalar intensity fields of the template and target images are denoted by T and S, respectively. The deformation map is $\boldsymbol{\varphi}(\boldsymbol{X}) = \boldsymbol{x} = \boldsymbol{X} + \boldsymbol{u}(\boldsymbol{X})$, where $\boldsymbol{x}$ are current (deformed) coordinates corresponding to $\boldsymbol{X}$ and $\boldsymbol{u}(\boldsymbol{X})$ is the displacement field. $\boldsymbol{F}$ is the deformation gradient:

$$\boldsymbol{F}(\boldsymbol{X}) = \frac{\partial \boldsymbol{\varphi}(\boldsymbol{X})}{\partial \boldsymbol{X}}. \tag{1}$$

The change in density is related to $\boldsymbol{F}$ through the Jacobian, $J := \det(\boldsymbol{F}) = \rho_0/\rho$, where ρ_0 and ρ are densities in the reference and deformed configurations, respectively. The left Cauchy-Green deformation tensor[22] is $\boldsymbol{C} = \boldsymbol{F}^T\boldsymbol{F}$. The Green (Lagrange) strain ($\boldsymbol{E}$) is defined as,

$$\boldsymbol{E}(\boldsymbol{X}) = \frac{1}{2}\left(\boldsymbol{C}(\boldsymbol{X}) - \boldsymbol{I}\right). \tag{2}$$

In hyperelastic warping, a spatial discretization of the template image is deformed into alignment with the target image. The target image remains fixed with respect to the reference configuration and does not change over the course of the analysis and is denoted as $T(\boldsymbol{X})$. The values of S at the material points associated with the template change as the discretized template deforms into registration with the static target image data set and is written as $S(\boldsymbol{\varphi})$. In other words, from the perspective of the material points associated with the discretized template image, the target intensity changes with deformation while the template intensity does not.

Hyperelastic warping can be posed as the minimization of an energy functional $E(\boldsymbol{\varphi})$ that consists of two potential energy terms:

$$E(\boldsymbol{\varphi}) = \int_{\beta} W(\boldsymbol{X},\boldsymbol{C})\frac{dv}{J} - \int_{\beta} U\left(T(\boldsymbol{X}),S(\boldsymbol{\varphi})\right)\frac{dv}{J}. \tag{3}$$

Here, W is the potential energy density associated with the *a priori* model and is typically selected to regularize the solution process and/or constrain the deformation map to have desirable characteristics such as ensuring diffeomorphic mappings. W is chosen to be the hyperelastic strain energy from continuum mechanics [22]. U is the image potential energy density. β denotes spatial domain of integration for the template in the deformed configuration. In hyperelastic warping, the image energy is represented as:

$$U(\boldsymbol{X},\boldsymbol{\varphi}) = \frac{\lambda}{2}\left(T(\boldsymbol{X}) - S(\boldsymbol{\varphi})\right)^2, \tag{4}$$

where λ is a penalty parameter that enforces alignment of the template model with the target image. The first variation of (3) corresponds to the weak form of the momentum equations for nonlinear solid mechanics (see, e.g., [23]). The first variation of the functional U in (4) in the direction $\boldsymbol{\eta}$ gives rise to the image-based force term:

$$DU(\boldsymbol{X},\boldsymbol{\varphi})\cdot\boldsymbol{\eta} = -\lambda\left[\left(T(\boldsymbol{X}) - S(\boldsymbol{\varphi})\right)\frac{\partial S(\boldsymbol{\varphi})}{\partial \boldsymbol{\varphi}}\cdot\boldsymbol{\eta}\right]. \quad (5)$$

This term drives the template deformation based on pointwise differences in image intensity and the gradient of the target intensity, evaluated at material points in the template model. Complete details of the methodology can be found in our previous publications.[12, 13]

Image Acquisition and Reconstruction. Dynamic PET image data were acquired using the microPET II at UC Davis. Three rats were imaged at approximately 10-week intervals. Each time a dose of 1-2 mCi of F-18 Fluoro-2-Deoxyglucose (^{18}FDG) was injected and gated list mode data of 600-900 million counts were acquired over 60-80 minutes. The list mode data were histogrammed into 8 gates of the cardiac cycle; summing the latter 50 minutes of the 80 minute acquisition for SHR 1 and summing all 60 minutes for SHR 2 and the WKY (normal control) acquisitions, resulting in identical times post injection. Images of 128×128×83 matrices of 0.39×0.39×0.58 mm^3 voxels in x, y, and z for each gate were reconstructed using 100 iterations of the iterative MAP reconstruction algorithm[24]. The projector and backprojector used a system matrix that modeled the solid angle effect, crystal penetration, intercrystal scatters, and the block structure of the microPET II. The MAP algorithm scales the weighting of the prior to keep the resolution constant throughout the image. The prior penalized the high frequency components of the reconstruction using appropriate weighting between 26 nearest neighboring voxels. The weighing of the prior was scaled so that the weighting between the prior and the likelihood function remained relatively the same from time frame to time frame as the counts changed in the data due to the wash-in and wash-out of ^{18}FDG from the myocardium. The end-systolic, mid-diastolic and end-diastolic image data set were determined through comparison of the gated image data with the ECG waveform. These images were rotated into long and short

axis orientations using MRIcro (www.mricro.com). Each image data set was reduced to 128×128×31 voxels.

FE Mesh Generation and Boundary Conditions for the Validation, Diastolic Model. The boundaries of the LV were obtained by manual segmentation of the epi- and endocardium from the template image for the WKY 6/18/2003 image data set. The 3-D FE model was constructed to include the entire image domain, with the tissue surrounding the myocardium represented as an isotropic hyperelastic material (tether mesh) with relatively soft properties (modulus of elasticity E = 0.3 KPa and Poisson's ratio ν = 0.3) so that the entire template image could be mapped (Fig. 1). The edges of the mesh were fixed to eliminate rigid body modes. An end-diastolic pressure load of 550 Pa (4.125 mmHg) was specified for the forward diastolic model.[25]

Constitutive Model and Material Coefficients. The myocardium was represented as a transversely isotropic hyperelastic material with the fiber distributions defined from literature values [26]. The transversely isotropic material represents nonlinear fibers embedded in an isotropic matrix. The strain energy W of this material model was represented as:

$$W = \mu(\tilde{I}_1 - 3) + F_2(\tilde{\lambda}) + \frac{K}{2}[\ln(J)]^2, \tag{6}$$

where the term $\mu(\tilde{I}_1 - 3)$ represents an isotropic neo-Hookean matrix material. $\tilde{I}_1$ is the first deviatoric invariant of $\boldsymbol{C}$ [22], $\tilde{\lambda} = \sqrt{\boldsymbol{a}_0 \cdot \tilde{\boldsymbol{C}} \cdot \boldsymbol{a}_0}$ is the deviatoric fiber stretch along the local direction $\boldsymbol{a}_0$, μ is the shear modulus of the matrix and K is the bulk modulus.

The fiber stress-stretch behavior was represented as exponential, with no resistance to compressive load:

$$\tilde{\lambda}\frac{\partial F_2}{\partial \tilde{\lambda}} = 0, \qquad \tilde{\lambda} < 1,$$
$$\tilde{\lambda}\frac{\partial F_2}{\partial \tilde{\lambda}} = C_3\left[\exp\left(C_4\left(\tilde{\lambda}-1\right)\right)-1\right], \qquad \tilde{\lambda} \geq 1. \tag{7}$$

Here, C_3 scales the stresses and C_4 defines the fiber uncrimping rate. A description of the constitutive model and its FE implementation can be found in Weiss *et al.* [27]

The material coefficients of the model (μ, C_3 and C_4) were determined by a nonlinear least squares fit of the transversely isotropic material to equibiaxial stress/strain curves presented in the literature [26] for the WKY rat left ventricle (μ = 2.10 KPa, C_3 = 0.41 KPa, and C_4 =22.0). A bulk modulus K of 100.00 KPa was used to define the myocardium as nearly incompressible.

Initial Validation of Strain Predictions from Hyperelastic Warping. The initial validation of warping was performed using synthetic image data set representing three known deformation states of the LV. A synthetic target image was created by applying the displacement map of the forward FE model to the template microPET image (Fig. 2) as was demonstrated in our previous work [13], creating mid- and end-diastolic image data sets.

The warping FE model used the same geometry and material properties as the forward FE model but without the tether mesh (Fig.1 right). The image data set were the only input for the warping analyses as pressure boundary conditions were not applied. Scatter plots of the fiber stretch (deformed length/reference length), circumferential, radial and longitudinal strains (eqn. (2)) were generated to determine coefficients of determination (R^2) between warping and forward FE model predictions. A Bland-Altman analysis was performed to assess agreement between the forward FE and warping predictions for the four measures of deformation and to identify possible bias in these predictions. The Bland-Altman analysis technique allows for the determination of the amount of agreement, bias and precision of two sets of data. It is a comparison of the differences between the data against the average of the measurements [28]. In

this case it was the average of the forward and warping nodal strains, which were compared with the differences between these nodal strain values.

Sensitivity Studies. The intensities of nuclear based images represent the relative uptake of the tracer, in this case of ^{18}FDG, by the tissue. A series of sensitivity studies were carried out to determine how variations in global tracer uptake would affect the strain distributions predicted by warping. In the first study, the intensities of the template and the target image data set were both reduced by 25%, 50% and by 75% (Fig. 3). In the second study, only the target image intensities were reduced by these amounts, while the template image was not altered. This study was repeated using histogram equalization during the analysis to balance the dynamic ranges of the template and target image data set. The third sensitivity study looked at regional reductions in image intensity, representing reduced uptake in a section of the myocardium such as might occur during ischemia. A section of the lateral freewall (Fig. 4) was created with reduced intensity (25%, 50% and by 75%) for both the template and target image data sets. The ischemic regions run the full length of the LV. The warping analysis was carried out on these image data sets using the same warping model as described above.

One of the primary limitations of finite element models of the left ventricle is that the material properties of the heart cannot be determined on a subject specific basis. Our previous work[13] has indicated that LV deformation results determined using hyperelastic warping were relatively insensitive to changes in material property coefficients when analyzing cine-MRI images of the heart. A sensitivity study was conducted to determine whether the warping analysis of the lower resolution nuclear images would show sensitivity to changes in material parameters. The values of μ and C_3 were increased and decreased by 20% [13] and the warping analysis of the validation model was repeated without altering any other aspect of the analysis.

The absolute RMS error between the forward nodal strains and the warping predicted nodal strains were used to compare the cases of altered uptake as well as the effects of variations in material properties.[29] The RMS error was calculated using:

$$\text{RMS error} = \sqrt{\frac{1}{N_{\text{nodes}}} \sum_{i=1}^{N_{\text{nodes}}} (\varepsilon_{\text{forward}} - \varepsilon_{\text{Warp}})^2}\ , \tag{8}$$

where $\varepsilon_{\text{Warp}}$ is the predicted strain value for the corresponding node in the warping analysis and N_{nodes} is the total number of nodes in the elements representing the myocardial wall.

Hyperelastic Warping Applied to Temporal gated microPET Image Data.

An application of warping to actual data is demonstrated through the analysis of image data from the two SHR and the single WKY rat which were acquired over the animals' respective lifetimes (Tables 1 and 2). These data were split into end-systolic, mid-diastolic and end-diastolic images and each image data set was aligned into long and short axis orientations. The ejection fractions were calculated for each microPET data set using methods developed for use with the imaging of small hearts as detailed by Feng *et al.*[30]

Hyperelastic warping was performed using the end-systolic images as the template image with the mid-diastolic and end-diastolic images being used as sequential target images providing an analysis of diastolic relaxation and filling. The movement of the base was easily determined through comparison of the aortic valve region of the template and target image data set and determining a relative displacement. This displacement was used as a boundary condition for the base of the warping model. The nodal strain data from each of the warping analyses were compiled and the average fiber stretch and first principal strains over the entire LV were calculated to determine if there was a global increase in strain between the subjects. The LV was divided into four equally spaced quadrants (lateral, anterior, septal and posterior) running the

length of the LV. The average strains for each quadrant were determined and the results were compared to see if there were any regional variations in the strain distributions.

Statistical Analysis of Rat Data

A fixed-effect, multi-factor, repeated measures Analysis of Variance (ANOVA) was performed considering first principal strain as the response variable. The following were used as the predictor variables, geometry (LV quadrant), treatment (SHR vs normal) and time (acquisition date). Mean values for the predictor variables were considered in the analysis (e.g. average strain within the quadrant).

Results

Hyperelastic Warping Validation

Comparison of Forward FE and Warping Predictions. There was excellent agreement between forward and warping predictions of 1st principal strain (Fig. 5). Regression analysis revealed significant correlations between the forward FE and warping predictions for fiber stretch (R^2 = 0.96), circumferential strain (R^2 = 0.96), radial strain (R^2 = 0.93), and longitudinal strain (R^2 = 0. 0.76) ($p<0.001$ for all cases) (Figs. 6A-D). The Bland-Altman analyses indicated that there was apparent bias in the fiber stretch (Bland-Altman regression slope of less than 0.02), while the circumferential, and longitudinal strains showed a slight tendency toward underestimation at the higher strain levels (Figs. 7A-D). Regression analysis of the Bland-Altman data indicated that the circumferential regression slope was -0.09 and the longitudinal regression slope was -0.19. A similar tendency for underestimation at higher strain levels was seen in the radial strain results (radial regression slope = 0.19).

Sensitivity to Global Decreases in Image Intensities. The predictions of fiber stretch and strain were insensitive to changes in image intensity when both the template and target images

were altered by the same amount (Table 3). A sharp degradation of the predicted strains (large increase in RMS error) could be seen when the image intensity of the target images were decreased while template images were left unchanged. Compensating for the difference in image intensities using histogram equalization resulted in RMS errors equal to those associated with the original validation analysis.

Sensitivity to Local Decreases in Image Intensities. The predictions of fiber stretch and the other measures of strain were insensitive to moderate changes in local image intensity (Table 3). However, the 75% reduction case did show a slight increase in RMS error associated with the strain predictions suggesting that larger reductions in regional uptake could result in increasing errors (Table 3).

Sensitivity to Changes in Material Parameters. Hyperelastic warping showed a slight sensitivity to changes in material coefficients for this application. There was a small increase in RMS error when μ and C_3 were altered (Table 4). Fiber strain showed the least sensitivity to changes in material coefficients while both the radial and longitudinal strains showed very similar increases in RMS errors compared with the validation model. The circumferential results showed more variability in the RMS errors with the μ-20% model showing less RMS error than the validation model while the largest increase in error was found the μ+20% model.

Image Data and FDG Uptake for microPET Data. The WKY rat showed a markedly different pattern of ^{18}FDG uptake over the life of the animal than the SHR subjects. The WKY rat showed lower ^{18}FDG uptake than the SHR for half of the first year of life, up to and including the 10/01/2003 study (Fig. 5). Subsequent microPET acquisitions of the WKY rat showed marked decrease in ^{18}FDG uptake with little or no uptake evident in the 2/11/2004, and the 9/21/2004 data set. The 4/27/2004 data set provided the final PET image of the WKY rat on

which subsequent strain analysis could be made. Both the 7/14/2004 and the 9/21/2004 WKY rat data set could not be used for strain analyses due to the lack of ^{18}FDG uptake in the LV wall. In contrast, the SHR subjects showed high ^{18}FDG uptake for the entire study, which decreased over the rats' lifespan. The 12/02/2004 SHR 2 data set could not be used for strain analysis due to problems with the list mode image acquisition.

SHR vs Normal Diastolic Function

Measures of Global Diastolic Function. Ejection fractions based on the microPET studies showed little difference between the SHR subjects and the WKY control (Fig. 8A). The control had an average ejection fraction of 67.9%, SHR 1 had an average ejection fraction of 66.00% and the SHR 2 had an average ejection fraction of 69.21%. Both the end-diastolic and end-systolic volumes were increased in the SHR subjects compared with the volumes of the normal control resulting in little difference in the ejection fractions (Table 2) between the types of rats. In contrast, the average 1st principal strain and average fiber stretch results indicated that the LV of the SHR subjects were undergoing greater deformation than the WKY rat (Fig. 8B and 8C). The control had an average 1st principal strain of 0.24, the SHR 1 had an average value of 0.29 and the SHR 2 had an average of 0.30. The fiber strain distributions showed a similar pattern with the control having an average fiber stretch of 1.08, SHR 1 had an average of 1.10 and the SHR 2 an average of 1.10. These results were confirmed in the regional analyses, particularly for the second year of life, where the highest strains were found, in general, in the lateral freewall (Fig. 10). In contrast, there was no distinct pattern as to which region would have undergone the greatest deformation during the first year of life. Similar trends were found for the radial, fiber and 1st principal strains (data not shown).

Statistical Analysis of Rat Data. The statistical results indicated that time and geometry (location in the LV) were significant ($p < 0.02$) while the other factors were not found to be significant. The analysis indicated that there was a significant interaction between time and treatment (SHR vs WKY) ($p = 0.03$).

Discussion

Hyperelastic Warping

The initial validation results indicate that hyperelastic warping can provide accurate predictions of LV deformation and strain during diastole in the case of the analysis of synthetic image data. The results indicated that the warping strain predictions were strongly correlated with the forward strain results upon which the image data sets were based. Furthermore, the intensity variation sensitivity study indicated that the technique was relatively insensitive to global changes in uptake. The global reduction of tracer uptake represents cases where the tracer uptake has been affected by changes in the subject's physiology. For example, medical conditions such as non-insulin dependent diabetes have been found to result in a marked decrease in ^{18}FDG by the heart[31, 32]. Yokoyama *et al.*[33] found that increased levels of insulin will also decrease the uptake of ^{18}FDG by the heart of hypertriglyceridemic patients.

Traditionally, regional variations in uptake of the heart are used to evaluate the viability of tissue [32, 34] following an ischemic episode. Those areas that show some uptake are considered viable with a reasonable expectation of some return of function following revascularization. Areas without uptake are considered to have a low likelihood for return of function as this is likely to be scar tissue[35-37]. The addition of a local ischemic region showed little effect on the predicted strain distributions compared with that of the forward model for the 25% and the 50% cases. The 75% ischemic model showed a slight increase in error. These results indicate a

limitation of the methodology. Since the warping forces that drive the deformation are provided by pointwise differences in image intensities between the template and target image data sets, the inclusion of a region with exceptionally low image intensity (<75% of normal) will result in the generation of vastly different warping forces in the normal regions compared with the reduced uptake regions. This has the potential to introduce error in the strain estimates within the reduced uptake regions since these regions would require higher penalties (equations (4) and (5)) to achieve proper image registration than the surrounding normal regions. Warping in its current form uses a globally applied penalty and so cannot accommodate such a vastly different penalty requirement. The methodology could be altered to accommodate cases where a position dependent penalty would be beneficial. The model would be unable to provide reasonable estimations of the tissue deformation in regions of the LV wall with no local uptake due to the lack of warping forces generated within these regions.

Warping predictions of fiber stretch and strain were relatively insensitive to changes in material properties μ and C_3. These results are consistent with our previous work, which illustrated the use of warping with cine-MRI image data sets in humans[13] and also found the technique to be relatively insensitive to changes in these same parameters. That work did show that warping was sensitive to altering the bulk behavior of the model. An order of magnitude decrease in the bulk modulus K resulted in an approximate doubling of the RMS errors. Though not repeated for this study, we would expect this exact behavior for warping using microPET imaging as the nearly incompressible behavior of the LV model is necessary for proper image registration of the model. This would be particularly true in regions of the LV wall with relatively homogenous intensity distributions. In other words, there is less image information to drive the registration.

It should be noted that the warping loads placed on the FE model are not physiological. They are simply the result of the local (element level) difference in image intensities that are used to define the warping body force that is used to deform the template mesh. Furthermore, while biaxial testing experimental data was used to fit the material coefficients, it is likely that in vitro testing does not capture the true behavior of the in vivo myocardium. However, this study has indicated that warping is relatively insensitive to changes in material properties so that errors in material property estimates becomes less of a concern compared with using these material property definitions in a standard forward FE model."

The methodology illustrated in this paper is not intended to replace validations based on the comparison with more common techniques for quantifying regional ventricular deformation such as tagged MRI analyses. It should be noted that these types of validations require that comparisons be made of image modalities and analysis techniques of differing spatial resolutions for the respective image data set, for example MRI and PET requiring that separate acquisitions be made. These issues make discerning the root cause(s) of any reported differences in displacement and strain difficult. Despite these drawbacks, such comparisons are underway.

Hyperelastic warping offers several advantages over other methods used to determine LV strain distributions. Unlike 2-D echocardiography, warping is fully 3D. 3D echocardiography is not commonly used to evaluate cardiac function although this may change in the future as it is the least invasive of the 3D imaging modalities available to evaluate cardiac function. Another strength of warping is that, unlike tagged MRI, it is not tied to a single imaging modality and has the potential to be able to analyze multi-modality images (e.g. PET-CT, SPECT-CT etc.).

The present results suggest that hyperelastic warping can provide accurate strain estimates from relatively low resolution image data such as microPET. As reported above, the

image data sets were 128x128x31matrices of 0.39 mm/voxel in-plane and 0.58 mm/voxel axially. The left ventricle wall for the WKY rat was approximately 10 voxels thick at the mid-ventricle. During the course of the warping analysis, the intensities of the template and target images are sampled based upon the mesh density of the model. In all of the studies presented, the LV depicted in the microPET image was sampled approximately every 0.25 mm radially and 0.75 mm circumferentially through most of the left ventricle. The apex was sampled with a higher spatial resolution since this region had approximately 5 times the mesh density as the remainder of the LV. All of the models used in the validation study as well as the SHR study had the same mesh densities. *Temporal Study of SHR and Normal Control Rats*

There was little difference in the LVEF for the SHR subjects and the WKY normotensive control. The SHR subjects showed higher average strains than the control in the first year of life. This is likely due to the LV relaxing from a greater contraction and increased diastolic volume from the increased filling pressures. These results are not surprising since at this point in the rats' life the passive behavior of the LV has not altered. With the onset of diastolic heart failure one would expect reduced filling volumes due to the stiffening of the LV. The difference in average strains would have been higher except for the decreased function measured in the SHR 1 during the 4/27/2004 acquisition. The decreased function seen at this acquisition was likely an adverse reaction to the anesthetic administered during the imaging.[38] Our results are similar to those of Cingolani *et al.*[15] who found that the LVEF of SHR and normotensive rats were very similar up to heart failure. Their results indicated that the increased diastolic pressure is compensated for by increased LV systolic work. This is in contrast to a temporal study of LV function by Kokubo *et al.* [39], who reported that after 8 weeks of age and up to 24 weeks the SHR had lower EF and fractional shortening than the normotensive control. Our data suggest that the

compensatory increase in systolic function occurs at 4-6 months of age and is maintained throughout the first year and a half of life and is illustrated by the increase in LV strain in the SHR animals. The primary result of the rat study suggests that there is a tendency in the second year of life for the lateral free wall of the SHR to undergo the largest deformation compared with the other regions of the LV. The WKY control also showed a similar tendency, but with lower deformation values overall than the SHR subjects. The statistical analysis indicated that the differences in average strains (Fig. 10) for the different LV quadrants were significant, however, the differences between the SHR and normal control rats were not . This is likely due to the fact that there were simply too few rats in the study. In the future, these experiments will be repeated with a minimum of 10 SHR and 10 WKY control rats.

The primary advantage of using radiolabeled tracers for the study of cardiac energy metabolism in humans and animal subjects is that it provides measurements of regional substrate uptake. Glucose, fatty acids, and acetate are the primary energy sources used by the heart with normal heart utilizing fatty acid oxidation as the primary energy source. Human, canine, and rodent studies show that in late-stage heart failure, there is down regulation of myocardial fatty acid oxidation and an increased reliance on glucose oxidation [40, 41]. However, the time course and the molecular mechanisms for this switch in substrate oxidation are not completely understood [42, 43]. A recent study by our group using dynamic microPET data indicated that metabolic rate of ^{18}FDG in the SHR subjects were far greater over the entire lifespan than WKY control animals [44], which had a metabolic rates less than half that of the SHR. While both types of rats showed the tendency for ^{18}FDG metabolism to decrease with time, in the normal WKY control metabolism of ^{18}FDG was so low as to not be measurable in the second year of life.

While providing valuable insight into the metabolic differences between the SHR and the WKY control, the lack of ^{18}FDG uptake in the normal control also represents the greatest limitation in the present study. Strain analysis could not be performed on the normal control because of the lack of usable microPET image data for most of the second year of life. Therefore, strain magnitude and distribution information for the aged WKY control were not obtained. The other notable limitation of this study is the lack of SHR measurements once the animals were in heart failure. While one acquisition did show LV hypertrophy, no measurements were made from the onset of heart failure to the death of the animals. The lack of ventricular stiffening during the non-failure period is not surprising since histological studies[45] indicate that the fibrosis responsible for ventricular stiffening occurs during heart failure rather than building gradually over the life of the subject. The expression of genes encoding extracellular matrix components, including collagen I, collagen III, and fibronectin in SHR subjects in heart failure were substantially higher than relative to age-matched WKY rats and non-failure SHR subjects.[46]

While providing insight into the temporal changes associated with hypertension in the SHR animal model, the small size of this study limits the extent to which conclusions can be made regarding the data. The study has too few animals and lacks a complete image data set for the control for its second year of life. Plans are underway to repeat this work with a tracer that can be effectively taken up by the LV of both the SHR and the normal control.

Conclusions

The present study indicates that hyperelastic warping can predict the strain distributions during diastole derived from synthetic microPET data sets and could be a valuable tool to determine cardiac function directly from nuclear images. The study further indicates that the

technique is insensitive to global changes in uptake as well as being insensitive to moderate changes in regional uptake. Increased errors were found in the case representing a large decrease in regional uptake (75%). The work also indicates that the technique was relatively insensitive to changes in material parameters. Overall, these results suggest that the technique may prove to be a relatively robust one when applied to nuclear imaging.

Acknowledgements

We want to thank Simon Cherry, Ph.D. for access to the microPET II at UC Davis and Kathleen Brennan, DVM of LBNL and Steve Rendig UC Davis for help with the animal studies. We also want to thank Thomas Ng bioengineering student at UC Berkeley for help with obtaining blood pressure measurements and Rod Gullberg of Washington State Patrol for his assistance with the statistical analyses. This work was supported in part by the Director, Office of Science, Office of Biological and Environmental Research, Medical Science Division of the U.S. Department of Energy under Contract No. DE-AC02-05CH11231 and in part by NIH grant number RO1 EB00121 awarded by the National Institute of Biomedical Imaging and Bioengineering and by NSF number grant BES-0134503.

References

1. Veress AI, Segars WP, Weiss JA, Tsui BM, Gullberg GT. Normal and pathological NCAT image and phantom data based on physiologically realistic left ventricle finite-element models. *IEEE Trans Med Imaging* 25(12):1604-16, 2006

2. Germano G, Kiat H, Kavanagh PB, et al. Automatic quantification of ejection fraction from gated myocardial perfusion SPECT. *J. Nuc. Med.* 36:2138-2147, 1995

3. Nakata T, Katagiri Y, Odawara Y, et al. Two- and three-dimensional assessment of myocardial perfusion and function by using technetium-99m sestamibi gated SPECT with a combination of count- and image-based techniques. *J. Nuc. Card.* 7:623-632, 2000

4. Faber TL, Cooke CD, Folks RD, et al. Left ventricular function and perfusion from gated SPECT perfusion images: an integrated method. *J. Nuc. Med.* 40(4):650-9, 1999

5. Zerhouni EA, Parish DM, Rogers WJ, Yang A, Shapiro EP. Human heart: tagging with MR imaging--a method for noninvasive assessment of myocardial motion. *Rad.* 169(1):59-63, 1988

6. Buchalter MB, Weiss JL, Rogers WJ, et al. Noninvasive quantification of left ventricular rotational deformation in normal humans using magnetic resonance imaging myocardial tagging. *Circ.* 81(4):1236-44, 1990

7. McVeigh ER, Zerhouni EA. Noninvasive measurement of transmural gradients in myocardial strain with MR imaging. *Rad.* 180(3):677-83, 1991

8. Axel L, Goncalves RC, Bloomgarden D. Regional heart wall motion: two-dimensional analysis and functional imaging with MR imaging. *Rad.* 183(3):745-50., 1992

9. Ungacta FF, Davila-Roman VG, Moulton MJ, et al. MRI-radiofrequency tissue tagging in patients with aortic insufficiency before and after operation. *Ann. Thorac. Surg.* 65(4):943-50, 1998

10. Epstein FH, Yang Z, Gilson WD, Berr SS, Kramer CM, French BA. MR tagging early after myocardial infarction in mice demonstrates contractile dysfunction in adjacent and remote regions. *Magn. Reson. Med.* 48(2):399-403, 2002

11. Sinusas AJ, Papdemetris X, Constable RT, et al. Quantification of 3-D regional myocardial deformation: shape-based analysis of magnetic resonance images. *American Journal of Physiology - Heart and Circulatory Physiology* 281:H698-H714, 2001

12. Veress AI, Weiss JA, Gullberg GT, Vince DG, Rabbitt RD. Strain measurement in coronary arteries using intravascular ultrasound and deformable images. *J. Biomech. Eng.* 124(6):734-41, 2002

13. Veress AI, Gullberg GT, Weiss JA. Measurement of Strain in the Left Ventricle during Diastole with cine-MRI and Deformable Image Registration. *J.Biomech. Eng.* 127(7):1195-1207, 2005

14. Bing OH, Conrad CH, Boluyt MO, Robinson KG, Brooks WW. Studies of prevention, treatment and mechanisms of heart failure in the aging spontaneously hypertensive rat. *Heart Fail. Rev.* 7(1):71-88, 2002

15. Cingolani OH, Yang XP, Cavasin MA, Carretero OA. Increased systolic performance with diastolic dysfunction in adult spontaneously hypertensive rats. *Hypertension* 41(2):249-54, 2003

16. Kobayashi T, Hamada M, Okayama H, Shigematsu Y, Sumimoto T, Hiwada K. Contractile properties of left ventricular myocytes isolated from spontaneously hypertensive rats: effect of angiotensin II. *J. Hypertens.* 13(12 Pt 2):1803-7, 1995

17. Zile MR, Brutsaert DL. New concepts in diastolic dysfunction and diastolic heart failure: Part II: causal mechanisms and treatment. *Circ.* 105(12):1503-8, 2002

18. Mandinov L, Eberli FR, Seiler C, Hess OM. Diastolic heart failure. *Cardiovasc. Res.* 45(4):813-25, 2000

19. Weber KT, Pick R, Jalil JE, Janicki JS, Carroll EP. Patterns of myocardial fibrosis. *J. Mol. Cell. Cardiol.* 21 Suppl 5:121-31, 1989

20. Ciulla M, Paliotti R, Hess DB, et al. Echocardiographic patterns of myocardial fibrosis in hypertensive patients: endomyocardial biopsy versus ultrasonic tissue characterization. *J. Am. Soc. Echocardiogr.* 10(6):657-64, 1997

21. Weiss JA, Rabbitt RD, Bowden AE. Incorporation of medical image data in finite element models to track strain in soft tissues. *SPIE* 3254:477-484, 1998

22. Spencer A. Continuum Mechanics. New York: Longman, 1980.

23. Marsden JE, Hughes TJR. Mathematical Foundations of Elasticity. Minneola, New York, 1994.

24. Qi J, Leahy RM, Cherry SR, Chatziioannou A, Farquhar TH. High-resolution 3D Bayesian image reconstruction using the microPET small-animal scanner. *Phys. Med. Biol.* 43(4):1001-13, 1998

25. Pacher P, Mabley JG, Liaudet L, et al. Left ventricular pressure-volume relationship in a rat model of advanced aging-associated heart failure. *Am. J. Physiol. Heart Circ. Physiol.* 287(5):H2132-7, 2004

26. Emery JL, Omens JH, McCulloch AD. Biaxial mechanics of the passively overstretched left ventricle. *Am. J. Physiol.* 272(5 Pt 2):H2299-305, 1997

27. Weiss JA, Maker BN, Govindjee S. Finite element implementation of incompressible, transversely isotropic hyperelasticity. *Comput. Meth. Applied Mech. Eng.* 135:107-128, 1996

28. Bland J, Altman D. Statistical methods for assessing agreement between measurement. *Biochimica Clinica*:399-404, 1987

29. Gonzalez R, Woods R. Digital Image Processing (3rd Ed.). New York: Addison-Wesley Publishing Company, 2006.

30. Feng B, Sitek A, Gullberg GT. Calculation of the left ventricular ejection fraction without edge detection: application to small hearts. *J. Nucl. Med.* 43(6):786-94, 2002

31. Voipio-Pulkki LM, Nuutila P, Knuuti MJ, et al. Heart and skeletal muscle glucose disposal in type 2 diabetic patients as determined by positron emission tomography. *J Nucl Med* 34(12):2064-7, 1993

32. Tamaki N, Yonekura Y, Yamashita K, et al. Positron emission tomography using fluorine-18 deoxyglucose in evaluation of coronary artery bypass grafting. *Am J Cardiol* 64(14):860-5, 1989

33. Yokoyama I, Ohtake T, Momomura S, et al. Insulin action on heart and skeletal muscle FDG uptake in patients with hypertriglyceridemia. *J Nucl Med* 40(7):1116-21, 1999

34. Tillisch J, Brunken R, Marshall R, et al. Reversibility of cardiac wall-motion abnormalities predicted by positron tomography. *N Engl J Med* 314(14):884-8, 1986

35. Wong CY, Tatini VR, Bis K. Combined CT-PET criteria for myocardial viability and scar: a preliminary report. *Int J Cardiovasc Imaging* 20(6):487-91, 2004

36. Haas F, Jennen L, Heinzmann U, et al. Ischemically compromised myocardium displays different time-courses of functional recovery: correlation with morphological alterations? *Eur J Cardiothorac Surg* 20(2):290-8, 2001

37. Delbeke D. Practical Fdg Imaging: A Teaching File. New York: Springer-Verlag, 2002.

38. Vanhove C, Lahoutte T, Defrise M, Bossuyt A, Franken PR. Reproducibility of left ventricular volume and ejection fraction measurements in rat using pinhole gated SPECT. *Eur J Nucl Med Mol Imaging* 32(2):211-20, 2005

39. Kokubo M, Uemura A, Matsubara T, Murohara T. Noninvasive evaluation of the time course of change in cardiac function in spontaneously hypertensive rats by echocardiography. *Hypertens Res* 28(7):601-9, 2005

40. Davila-Roman VG, Vedala G, Herrero P, et al. Altered myocardial fatty acid and glucose metabolism in idiopathic dilated cardiomyopathy. *J. Am. Coll. Cardiol.* 40(2):271-7, 2002

41. Sack MN, Rader TA, Park S, Bastin J, McCune SA, Kelly DP. Fatty acid oxidation enzyme gene expression is downregulated in the failing heart. *Circ.* 94(11):2837-42, 1996

42. Lehman JJ, Kelly DP. Gene regulatory mechanisms governing energy metabolism during cardiac hypertrophic growth. *Heart Fail. Rev.* 7(2):175-85, 2002

43. Stanley WC, Chandler MP. Energy metabolism in the normal and failing heart: potential for therapeutic interventions. *Heart Fail. Rev.* 7(2):115-30, 2002

44. Gullberg G, Huesman R, Qi J, Reutter B, Sitek A, Yang Y. Evaluation of cardiac hypertrophy in spontaneously hypertensive rats using metabolic rate of glucose estimated

from dynamic microPET image data. *The Society for Molecular Imaging, September 9-12, 2004, St. Louis, MO., Mol Imaging* 3:225, 2004

45. Conrad CH, Brooks WW, Hayes JA, Sen S, Robinson KG, Bing OH. Myocardial fibrosis and stiffness with hypertrophy and heart failure in the spontaneously hypertensive rat. *Circ.* 91(1):161-70, 1995

46. Boluyt MO, O'Neill L, Meredith AL, et al. Alterations in cardiac gene expression during the transition from stable hypertrophy to heart failure. Marked upregulation of genes encoding extracellular matrix components. *Circ. Res.* 75(1):23-32, 1994

Figure Captions

Figure 1. Left - Forward FE model used to create target image. Right – Detail of the LV with tether mesh removed. Warping models do not have tether mesh and can be represented by the figure on the right.

Figure 2. A mid-ventricular slice taken from (A) the template image data set and (B) the mid-diastolic image data set (target) and the (C) end-diastolic image data set (target) used in the validation study. The template image is from the SHR 2 6/18/2003 acquisition. The mid-diastolic and end-diastolic image data set were created using the displacements predicted by the forward FE model.

Figure 3. Mid-ventricular short axis slices from (A) the validation target image, (B) the target image with 25% global reduction in intensity levels, (C) the target image with 50% reduction in intensity levels, and (D) the target image with 75% reduction in intensity levels.

Figure 4. Mid-ventricular short axis slices from (A) the target image with 25% reduction in intensity levels in a region of the lateral freewall, (B) the target image with 50% reduction in intensity levels in this region, and (C) the target image with 75% reduction in intensity levels.

Figure 5. Forward and warping Green-Lagrange strain distributions show excellent agreement. (A) Location of the cross-sections, (B) 1^{st} principal strain cross-sections for forward model and (C) the 1^{st} principal strain cross-sections for warping model.

Figure 6. Scatter plots of forward FE versus warping stretch and Green-Lagrange strains indicate excellent agreement with R^2 values ranging from 0.76 to 0.96. (A) fiber stretch (final length/initial length), (B) circumferential strain, (C) radial strain, and (D) longitudinal strain. There are 4794 data points.

Figure 7. Bland-Altman plots of the validation stretch and strain comparisons. (A) fiber stretch, (B) circumferential strain, (C) radial strain (D) longitudinal strain. The plots show good agreement between the forward and warping solutions with a slight tendency for underestimation of fiber stretch, circumferential, and longitudinal strains at the higher strain levels. A similar tendency for underestimation can be seen in the radial strain results. The central solid line indicates the mean difference in the data while the heavy dashed lines indicate the boundary of ± 2 standard deviations.

Figure 8. FDG short axis end-diastolic images for the temporal study, (top) SHR 1, (middle) SHR 2, and (bottom) WKY rat. Each short axis slice is from the same mid-ventricular region. Panels without a clearly visable LV indicate little or no uptake in the WKY or in the case of the SHR 2 2/11/04 data set where end systole was not imaged. SHR 1 9/21/2004 data set shows the hypertrophic myocardium.

Figure 9. (A) Ejection fraction results indicate little discernable difference between SHR and the WKY normal rat. The (B) fiber stretch and (C) 1st principal strain results show higher values for SHR compared with the normotensive control. The fiber stretch and 1st principal strains are averages for the entire LV.

Figure 10. Temporal change in regional circumferential strain distributions for (A) WKY normal, (B) SHR 1 and (C) SHR 2. These results indicate that the strains in the SHR LV are higher for all regions after the second acquisition. Similar trends were found for the radial, fiber and 1st principal strains. These values represent the average circumferential strain for that quadrant. In other words the anterior strain in the figure is the average of all of the strain values within the region running the full length of the LV.

Tables

Rat	Age at death (months)	Blood Pressure (mmHg)	Ratio of Heart to Body Weight
Normal	24.5	154 (07/13/04)	0.0039
SHR 1	22.2	167 (07/13/04)	0.0063
SHR 2	21.7	165 (07/13/04)	

Table 1 Measured blood pressure and life spans of subjects. The WKY normal control rat was sacrificed while the SHR rats died of heart failure. The ratio of the heart to body weight data indicates that the SHR subject had a higher ratio which was due to both an increased heart size of the SHR compared with the normal control and the decrease in the SHR body weight compared with the normal control. The heart to body weight ratio for SHR 2 was not obtained due to the inadvertent disposal of the animal following its death.

Rat	Acquisition Dates	Age (months)	End-dias. Vol. (ml.)	End-sys. Vol. (ml.)	EF	Weight (grams)
Normal	6/18/2003	2.14	0.20	0.05	0.75	217
	8/6/2003	3.75	0.10	0.02	0.78	322
	10/1/2003	5.70	0.14	0.14	0.68	400
	12/2/2003	7.62	0.43	0.12	0.72	423
	2/11/2004	9.96	---	---	---	453
	4/27/2004	12.45	0.33	0.09	0.73	480
	7/14/2004	15.01	0.29	0.09	0.86	476
	9/21/2004	17.28	---	---	----	449
SHR 1	6/18/2003	2.14	0.22	0.07	0.66	254
	8/6/2003	3.75	0.11	0.03	0.73	327
	10/1/2003	5.70	0.44	0.13	0.71	380
	12/2/2003	7.62	0.45	0.15	0.67	394
	2/11/2004	9.96	0.46	0.16	0.64	407
	4/27/2004	12.45	0.36	0.18	0.49	425
	7/14/2004	15.01	0.41	0.13	0.70	406
	9/21/2004	17.28	0.47	0.20	0.58	395
SHR 2	6/18/2003	2.14	-----	-----	-----	-----
	8/6/2003	3.75	0.12	0.04	0.70	335
	10/1/2003	5.70	0.43	0.16	0.63	391
	12/2/2003	7.62	0.42	0.10	0.76	413
	2/11/2004	9.96	0.47	0.16	0.66	450
	4/27/2004	12.45	0.39	0.10	0.75	458
	7/14/2004	15.01	0.37	0.13	0.66	430
	9/21/2004	17.28	0.44	0.17	0.61	435

Table 2 The end-diastolic and end-systolic volumes of the SHR rats were consistently higher than the values for the WKY normal control. However, the ejection fractions for these acquisitions were not appreciably different between the SHR rats and the WKY normal control.

Target Image Data Set	Fiber strain	Circ. strain	Radial strain	Long. Strain
validation study	0.031	0.075	0.028	0.054
25% reduction	0.032	0.068	0.029	0.063
50% reduction	0.032	0.068	0.029	0.063
75% reduction	0.031	0.072	0.028	0.054
25% target reduction	0.054	0.533	0.076	0.252
50% target reduction	0.055	3.590	1.398	0.257
75% target reduction	0.574	4.56	1.40	1.216
25% target reduction Hist.	0.033	0.062	0.032	0.068
50% target reduction Hist.	0.033	0.061	0.032	0.068
75% target reduction Hist.	0.031	0.071	0.031	0.051
25% ichemic reduction	0.031	0.040	0.029	0.058
50% ichemic reduction	0.030	0.054	0.032	0.058
75% ichemic reduction	0.036	0.089	0.044	0.071

Table 3 The RMS error results suggest that warping does not appear to be sensitive to reductions in intensity levels when both the template and target images have an equal reduction in intensity. Increased errors are found in the case where the target image intensities are reduced and the template intensities remain unchanged. Histogram equalization (denoted as "Hist." above) successfully compensates for this case, resulting in errors similar to the validation errors. The ischemic region analyses indicate that the presence of an ischemic region in the lateral wall does not increase the error measures though the 75% ischemic model did show an increase in the RMS error.

Target Image Data Set	Fiber strain	Circ. strain	Radial strain	Long. Strain
validation study	0.031	0.075	0.028	0.054
μ-20%	0.031	0.066	0.036	0.075
μ+20%	0.031	0.098	0.039	0.072
C_3-20%	0.032	0.086	0.038	0.073
C_3+20%	0.032	0.077	0.039	0.071

Table 4 Warping appears to be relatively insensitive to changes in material parameters as indicated by the RMS errors shown above. The alterations in the shear modulus μ and C_3 did show some increase in the error measure particularly for the μ+20% case.

Figure 1

Click here to download Figure: figure1.eps

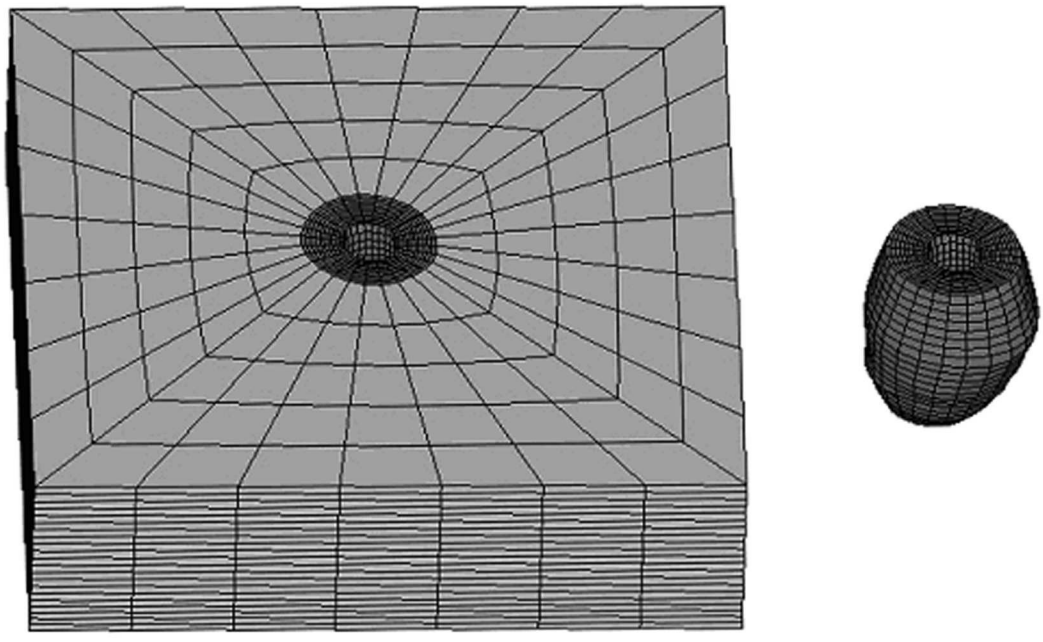

Figure 2

Click here to download Figure: figure2.eps

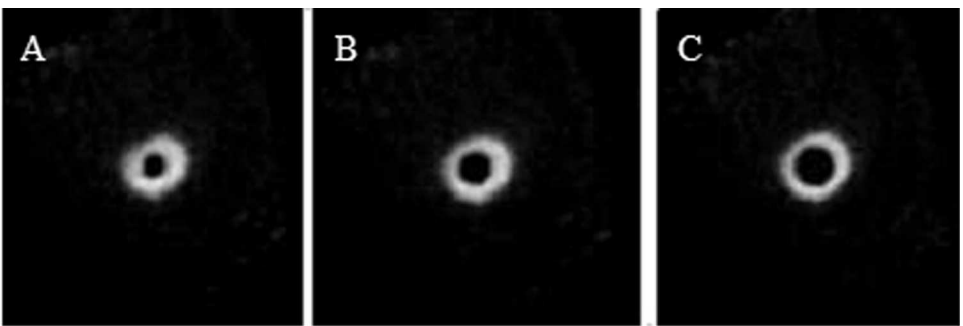

Figure 3

Click here to download Figure: figure3.eps

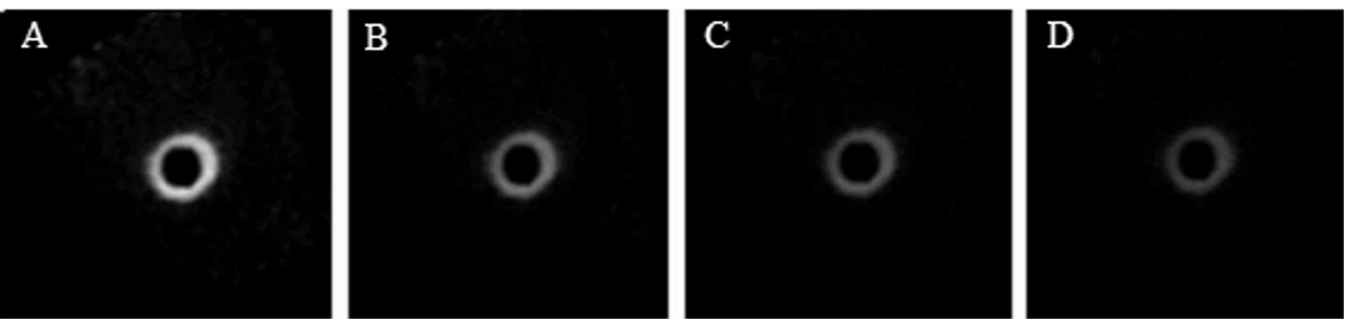

Figure 4

Click here to download Figure: figure4.eps

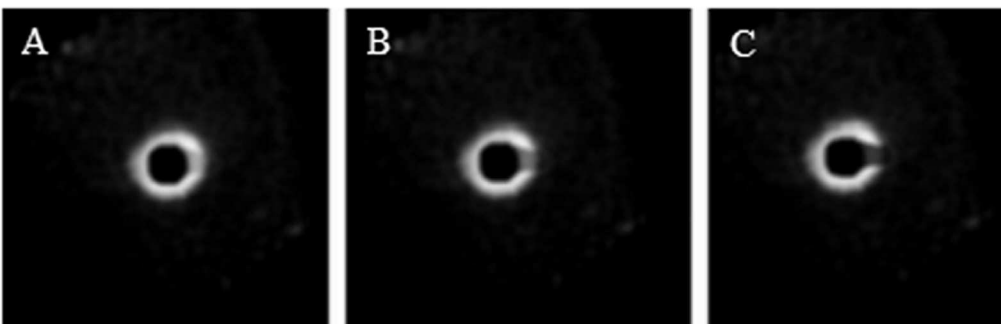

Figure 5

Click here to download Figure: figure5.eps

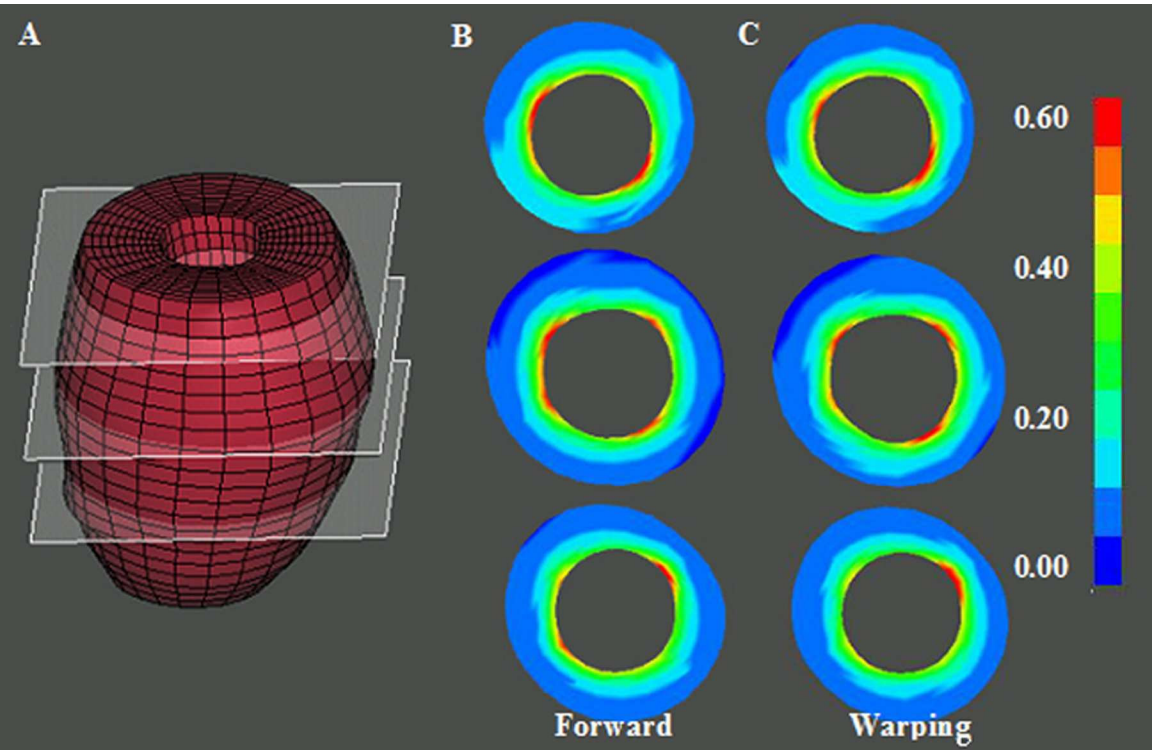

Figure 6

Click here to download Figure: figure6.eps

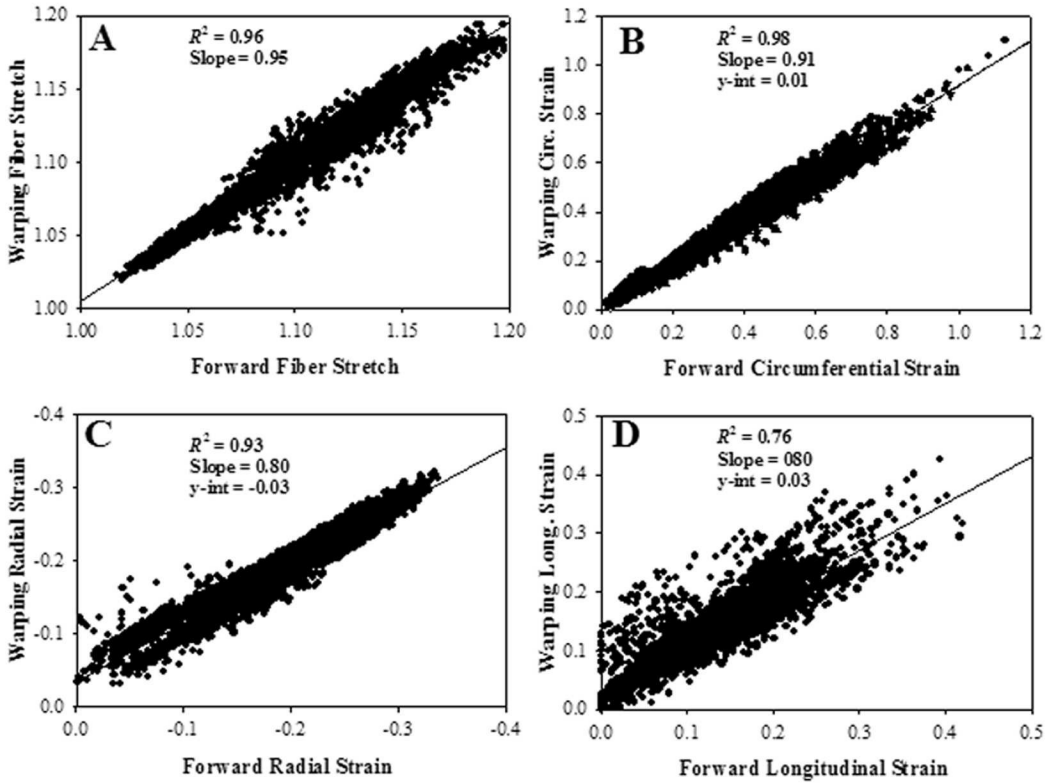

Figure 7

Click here to download Figure: figure7.eps

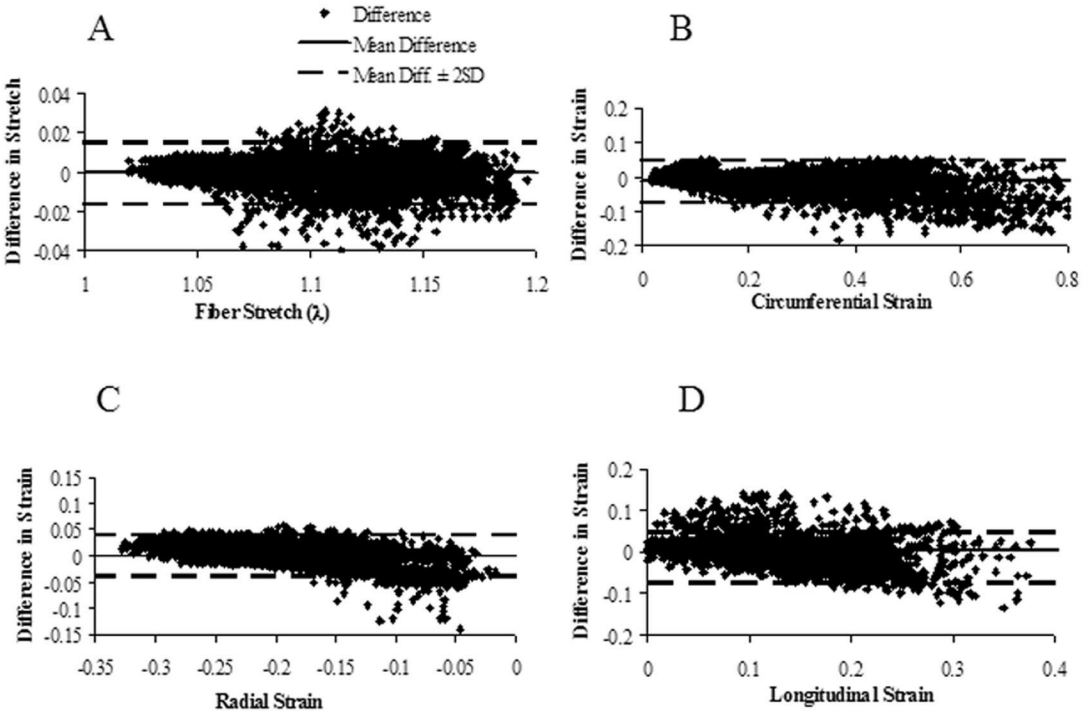

Figure 8

Click here to download Figure: figure8.eps

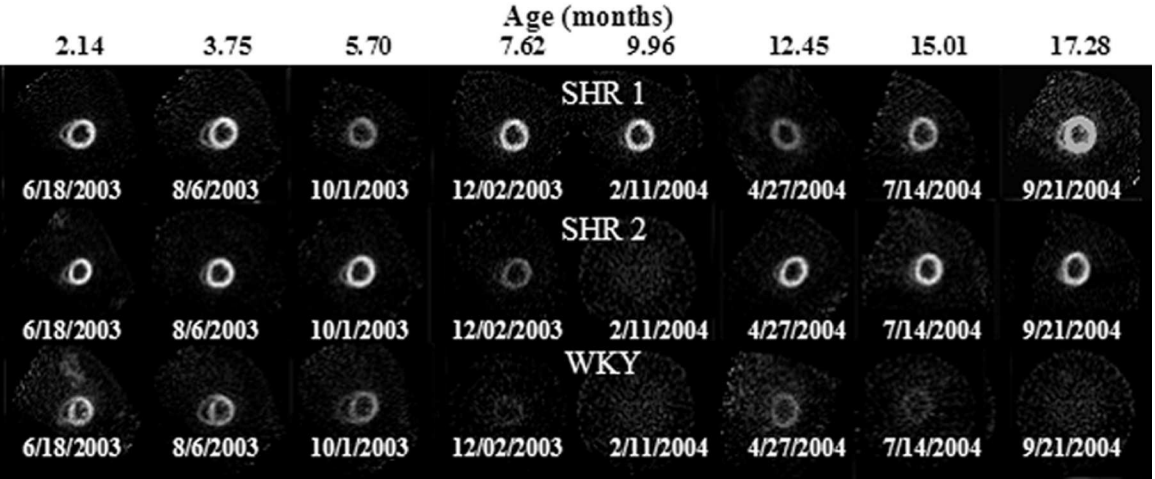

Figure 9

Click here to download Figure: figure9.eps

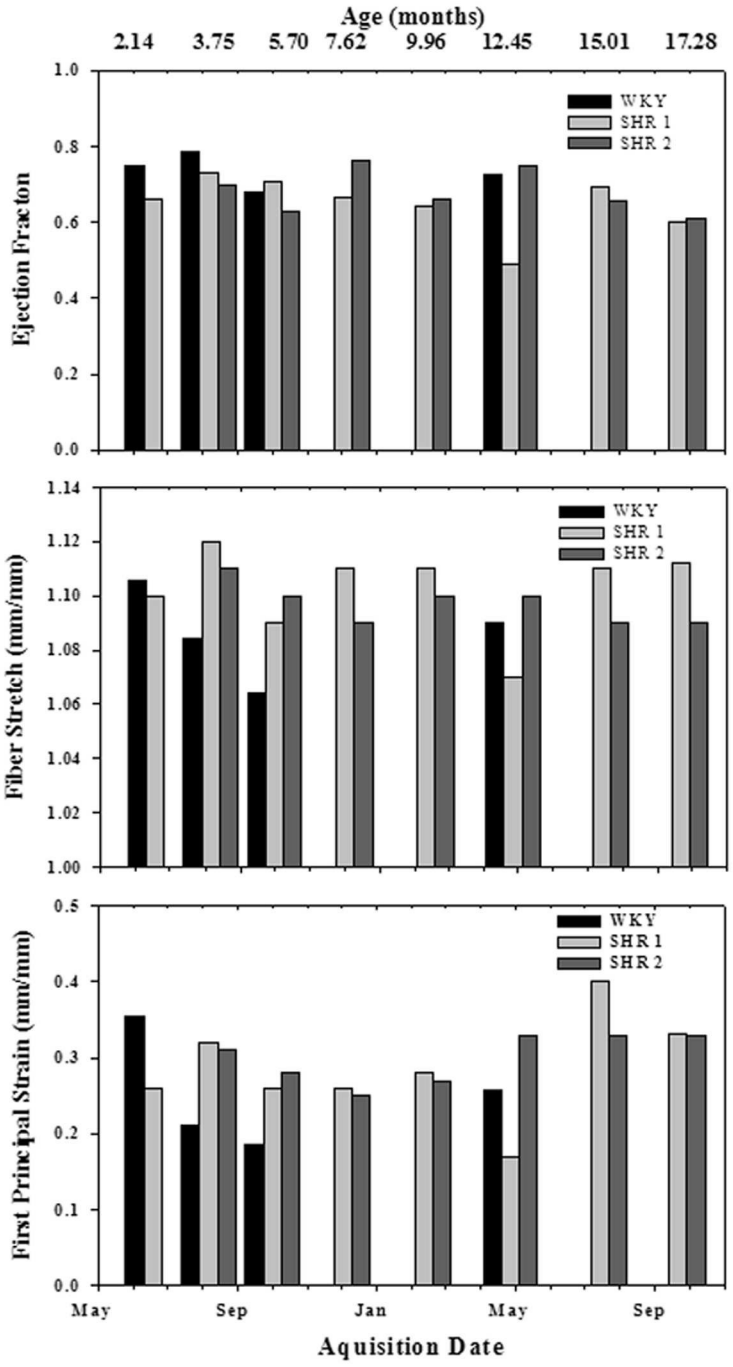

Figure 10

Click here to download Figure: figure10.eps